ORIGINAL PAPER

Titanium phosphates as positive electrode in lithium-ion batteries: composition, phase purity and electrochemical performance

Adel Attia · Qiong Wang · Xingkang Huang · Yong Yang

Abstract Titanium phosphate materials were synthesized by evaporation-induced self assembly method by using $Ti(OC_4H_9)_4$ and PCl_3, in the presence of Pluronic (P123) as a non-ionic surfactant template. The molar ratios of P/Ti and the heat treatment of the materials affected their structures, particle geometries and electrochemical performances as indicated by X-ray powder diffraction, thermal gravimetric analysis, scanning electron and transmission electron microscopy and other electrochemical techniques. As expected, increasing the temperature to 800 °C for 3 h resulted in losing the mesoporosity and generally led to a decrease in capacity of these materials. Cyclic voltammetry showed that TiP_2O_7 is formed at 500 °C for 10 h at a molar ratio P/Ti=0.412 as amorphous phase. On the other hand, at molar ratio P/Ti=2.06 showed sharp peaks indicated TiP_2O_7 transformed into crystalline material showed lower peak separation potential indicated that kinetic reactions might be favored.

Adel Attia is on leave from the National Research Centre, El-Buhooth St., Dokki 12311, Cairo, Egypt.

A. Attia · Q. Wang · X. Huang · Y. Yang
State Key Laboratory for Physical Chemistry of Solid Surfaces,
College of Chemistry and Chemical Engineering,
Xiamen University,
Xiamen 361005, China

A. Attia · Q. Wang · X. Huang · Y. Yang (✉)
Department of Chemistry, College of Chemistry and Chemical Engineering, Xiamen University,
Xiamen 361005, China
e-mail: yyang@xmu.edu.cn

A. Attia (✉)
Department of Physical Chemistry, National Research Centre,
El Buhouth St., Dokki,
12311 Cairo, Egypt
e-mail: adel_attia@hotmail.com

Introduction

The discovery of silicious material M41S family by Mobil researchers [1, 2] and its related members in 1992, featured by ordered mesoporous structure and sharp pore size distribution, led to surged interest in porous silicious and non-silicious materials as well. Mesoporous materials have taken extensive attention due to their involvement in diversity of applications including, for example, catalysis [3, 4], sensors [5, 6], host materials for lithium-ion storage [7–10], hydrogen production [11, 12] and storage [13, 14], electrochromic windows [15, 16], and dye-sensitized solar cells [17–19].

The breakthrough [20–22] reporting the possibility of using of olivine $LiFePO_4$ as cathode material in lithium-ion batteries as stable electrode has led to intensive and focus research on metal phosphates in general and on lithium iron phosphate in particular [10, 23–27]. In general, the major drawbacks of the majority of metal phosphate materials for lithium-ion batteries application are their low electronic conductivity, which renders their usage inapplicable. However, this problem could be solved by the addition of electronic conductor, such as, active carbon [22, 28, 29] or through synthesis of the metal phosphate materials in the mesoporous range which can also improve the ionic conductivity of the materials [30, 31].

Many attempts were tried to synthesize mesoporous titanium phosphates (TPs) by using different kinds of surfactants as templates. For instance, cetyl trimethyl ammonium bromide as a cationic surfactant, was used to synthesize high surface area of TP with mesoporous

structure [31], anionic surfactants were used as templates to synthesize mesoporous TPs which were only stable up to 300 °C [32], hydrothermal synthesis by using organic molecules in fluorinated media was successful to obtain a TP [33], a long chain alkylamine was reported to be used as a surfactant in synthesize a mesoporous TP [34] while a non-ionic surfactant route applied to synthesize stable and relatively high BET surface area (~250–350 $m^2 g^{-1}$) mesoporous titanium oxo phosphate [35]. Mesoporous Ti-MCM-41 functionalized with phosphate group by treatment with $POCl_3$ which affected the textural properties of the Ti-MCM-41(P) [36] is another example showing the applicability and significance of mesoporous TP.

To sum up, up-to-date different synthetic protocols affected the surface properties and hence the behavior of electrodes for different applications. In this work, we aimed at investigating different titanium phosphates and their electrochemical performance with regard to their application as positive electrodes in lithium-ion batteries.

Experimental section

Titanium phosphate synthesis and characterization

Samples were prepared by a modified copolymer surfactant, EO20-PO70-EO20, Pluronic (P123) template method [10]. The protocol of synthesis included dissolving of 4.5 g of P123 in appropriate volume of ethanol by the help of ultrasonication, titanium tetrabutoxide $(Ti(OC_4H_9)_4)$ added to the above solution followed by the addition of 4.12 g of PCl_3 slowly and dropwise. The above mixture was allowed to mix through stirring and was kept at 40 °C in oil bath to ensure a complete reaction for a day, at least. The obtained sol was poured into Petri dishes and was left in air to allow its transformation into a gel at room temperature for about 2–3 weeks. Two different molar ratios of P/Ti were prepared, viz., 0.412 and 2.06. The samples were dried gradually at 40, 60 °C and then at 80 °C for 2 h each prior to final calcination at 120 °C for 1–2 days. Then, the samples were divided into two groups, the first group heated at 500 °C for 10 h in air while the second group heated at 800 °C for 3 h in air. All samples were dried first at 120 °C before starting thermogravimetric–differential thermal analysis experiments which were carried out by using an STA 409 PC analyzer (Netzsch, Germany) at a heating rate of 10 °C min^{-1} under the flow of N_2 (40 mL min^{-1}).

Fourier-transform infrared (FTIR) spectra were recorded on an Avatar 360 spectrophotometer (Nicolet, USA). The spectra were recorded by using a pressed disc technique in which a sample and KBr were mixed thoroughly using an agate pestle and mortar in the approximate ratio of 1:25, respectively, then this mixture was compressed by using stainless steel molds. The spectral resolution of measurements was done by selecting the spectra every 2-cm^{-1} intervals over the wavenumber range measured.

X-ray diffraction experiments were carried out by a PANalytical X-pert diffractometer (Philips, Netherlands) using CuK_α radiation at 40 kV and 30 mA, the 2θ was in the range of 10 to 90 degrees for wide-angle X-ray diffraction (WAXRD) while it was from 0.5 to about 5 degrees for small-angle X-ray diffraction (SAXRD).

Scanning electron microscopy (SEM) studies were performed on LEO1530 (LEO company, Germany). Prior to mounting the samples to a vacuum chamber, the samples were mounted on a holder by fixing it to a double binder carbon tape, then sputtered with gold to enhance the conductivity of the samples. On the other hand, high-resolution transmission electron microscopy (TEM) images were obtained on an instrument of Philips-FEI Tecnai-F30 electron microscopy operating at 300 kV. Samples were ultrasonicated in ethanol prior to mount them on a copper grid coated with a polymer-supported film and carbon.

Electrode fabrication and cell assembly

The cathodes were prepared by mixing 80% of the active material with 10% carbon black and 10% polyvinylidene fluoride. This mixture was made into a slurry using 1-methyl-2-pyrrodinone solvent as a solvent by the assistance of a ball milling at 500 rpm for a minimum of 3 h. Aluminum foils, used as current collector, were roughened by using emery paper of 320 grade, then pre-treated in an ultrasonic bath of 0.1 M NaOH followed by washing with bidistilled water and then in an ultrasonic bath of 0.1 M oxalic acid for 10 min each, washed thoroughly with double-distilled water, then dried in an oven prior to loading of the cathode material. The electrodes were then coated onto Al foils by doctor blade method. They were left in an oven to dry at 120 °C for a minimum of 2 h under vacuum. Thereafter, the dried slurry was pressed on the Al current collector at 20 MPa to allow a good mechanical and electrical contact with the Al foil. The electrochemical properties of the synthesized samples were assessed by using CR2025 coin cells. The coin cells were assembled with the cathode as prepared, lithium metal as anode, and Celgard 2300 film as separator. The electrolyte was 1 M $LiPF_6$ dissolved in ethylene carbonate (EC) and dimethyl carbonate (DMC) mixture (1:1 by volume). The cells were assembled in an argon-filled glove box (mBraun model 100 G, Germany), where water and oxygen concentrations were kept around 1–2 ppm.

Electrochemical testing

Charge–discharge experiments were performed with current density and voltage range as defined later using a LAND CT2001A battery tester (Wuhan, China). The active mass of all the positive electrodes was in the range of 1–3 mg.

Cyclic voltammetry experiments were performed with conventional potentiostat instrument (EG&G PAR 263A). Electrochemical measurements were carried out in a one-compartment cell using lithium metal strips as reference and auxiliary electrodes, hence, all potentials are referred to the Li/Li$^+$ electrode, and the cathodes prepared as described above. The electrolyte was 1 M LiPF$_6$ dissolved in EC+DMC (1:1 volume ratio). The cell was assembled in an argon-filled glove box (mBraun, Germany), where water and oxygen concentrations were kept less than 2 ppm, and then sealed well with a paraffin wax and moved outside the glove box to carry out the measurements. In all cyclic voltammetry experiments, the direction of the first potential sweep was (1) equilibrium potential, (2) lower vertex potential, and (3) upper vertex potential.

Results and discussions

Titanium phosphate or related materials were synthesized by an evaporation-induced self-assembly method by using Ti(OC$_4$H$_9$)$_4$ and PCl$_3$, in the presence of Pluronic (P123) as a non-ionic surfactant template. During synthesis, two different molar ratios of P/Ti and two different heat treatments after samples being synthesized were used. The samples synthesized at P/Ti=0.412 (sample P-a) and at P/Ti=2.06 (sample P-b) were heat-treated at 500 °C for 10 h, while samples synthesized using P/Ti=0.412 (sample P-c) and at P/Ti=2.06 (sample P-d) were heat-treated at 800 °C for 3 h. More details concerning the synthesis protocol can be found in details in the experimental section. Before heat treatment, all samples were dried at 120 °C and analyzed by using thermal gravimetric analysis (TGA) and differential thermal gravimetric (DTG) as depicted in Fig. 1.

It is obvious that TGA curves can be categorized into three distinctive regions: the first region positioned below 200 °C and is characterized by gradual weight loss which is attributed to desorption of physically adsorbed water while the second region located nearly at 200–400 °C and characterized by fast weight loss which is assigned mainly to the loss of the remaining template (P123) which could not be removed completely in the drying process; in this region it is highly probable that transformation of orthophosphoric to pyrophosphoric acid starts to occur. The third region is
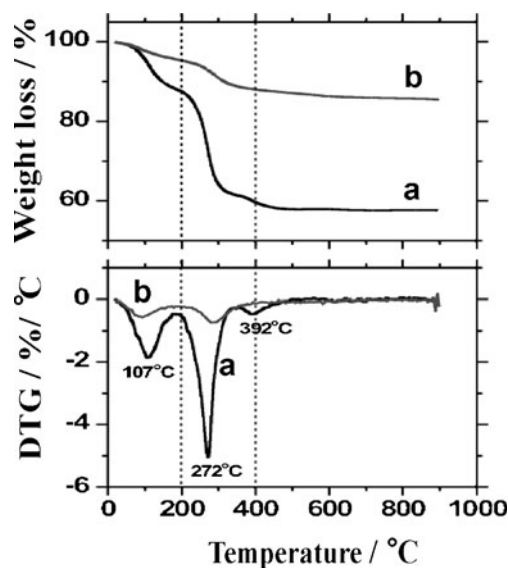

Fig. 1 TGA–DTG of the titanium phosphate materials after dried at 120 °C for 2 days. Titanium phosphate synthesized by using different molar ratio of P/Ti=0.412 (**a**) and P/Ti=2.06 (**b**)

located above ~400 °C which is characterized by a slight or no weight loss indicating a thermal stability of the materials in this region.

Moreover, DTG analysis of Fig. 1 shows that there is a sharp weight loss around 107, 272, and 392 °C, which can be attributed to loss of surface-bound water, template burning to carbon accompanied by orthophosphoric acid to pyrophosphoric acid transformation, followed by transformation of pyrophosphoric acid into metaphosphonic acid, respectively. The step around 392 °C was manifested more when the P/Ti molar ratio was 0.412 (dried at 120 °C for 1–2 days, curve a). This manifestation suggests that the phosphorus precursors did not react entirely to form TP compounds (vide infra). Accordingly, the free (unreacted) PCl$_3$ can explain a remarkable transformation into pyrophosphoric acid and then into metaphosphonic acid according to Eqs. 1–3. However, by increasing the P/Ti molar ratio, (2.06 calcinated at 120 °C for 1–2 days, curve b) we might have the same products with different kinetics which rely on the amount of free PCl$_3$. This is manifested by the intensity of peaks at 272 and 392 °C.

PCl$_3$ can be easily hydrolyzed to phosphonic acid, and hydrochloric acid is produced (Eq. 1) which is important to keep the pH lower (acidic) for the hydrolysis of titanium butoxide in the presence of PCl$_3$.

$$PCl_3 + 3H_2O \rightleftarrows H_3PO_3 + 3HCl \qquad (1)$$

Then phosphonic acid disproportionates when heated to form orthophosphoric acid according to Eq. 2

$$4H_3PO_3 \overset{\Delta}{\rightleftarrows} PH_3 \uparrow + 3H_3PO_4 \qquad (2)$$
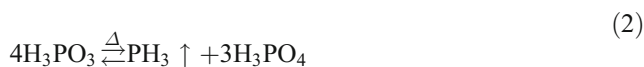
The pyrophosphoric acid is followed by its transformation into metaphosphonic acid (evidenced by the detection of the peak at 392 °C of DTG curves). This can be described [36] according to Eq. 3:

$$H_3PO_4 \underset{260°C}{\overset{}{\rightleftharpoons}} H_4P_2O_7 \underset{300°C}{\overset{}{\rightleftharpoons}} (HPO_3)_n \qquad (3)$$
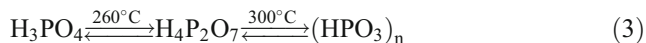
However, titanium pyrophosphate (TPP) or other phosphate derivatives formed instead of the pyrophosphoric acid upon the reaction with titanium precursor as will be discussed later. Some of this pyrophosphoric acid existed in excess with no involvement in reaction which is dependent on the amount of P/Ti molar ratio used. The excess of pyrophosphoric acid can be transformed into metaphosphonic acid at around 300 °C according to Eq. 3. The choice of heat treatment to be higher than 450 °C is on the base of the TGA.

Figure 2 shows the FTIR spectra of all prepared samples. All samples showed characteristic bands around 2,344 cm^{-1} assigned previously either to the presence of phosphorus acid or ester P–H stretching detected at 2,425–2,325 cm^{-1} [37]. Presence of the phosphorus acid and ester P–H can be existed and could be explained according to reaction (4):

$$PCl_3 + 3C_2H_5OH \rightleftharpoons HPO(OC_2H_5)_2 + C_2H_5Cl + 2HCl \qquad (4)$$

Since ethanol was used in significant amount to dissolve the co-polymer non-ionic surfactant (P123) used in this work, the presence of ester at either 500 °C for 10 h or 800 °C for 3 h could be explained. It seems impossible that ester could exist; the sole way to explain its

presence at such relatively high temperature is that it might be trapped in the pores due to condensation phenomenon (ink-bottle geometry of the pores, data not shown here).

Samples P-a and P-b showed bands at 1,646 and 1,630 cm^{-1} (Fig. 2a, b, respectively) assigned to H–O–H bending vibration from the structural water and the peak intensities of these bands were diminished in the direction of increasing of P/Ti molar ratio which suggests that the amount of the structural water is inversely related to P/Ti molar ratio. Lowering the P/Ti molar ratio favors the formation of TiO$_2$ in the samples at 500 °C for 10 h (confirmed later by X-ray diffraction (XRD) analysis as shown below), this behavior is in agreement with work reported previously that the increase of titanium ions in a tetrahedral coordination is more effective in adsorbing water [38].

The band appeared at 1,457 cm^{-1} exclusively for sample P-a, at P/Ti=0.412 molar ratio (Fig. 2a), could not be attributed to the deformation of –CH$_2$ and –CH$_3$ of the P123 copolymer, used as the template in this work, as evidenced from the TGA (Fig. 1), instead it can be ascribed to the Brönsted acidity due to the presence of P(OH)$_2$ groups [39]. The main band appeared at around 1,055 cm^{-1} (Fig. 2a) is usually assigned to Ti–O–P skeletal stretching vibrations [32, 40, 41]. Since Bhaumik and Inagaki [32] could not find this peak for mesoporous TiO$_2$ and this band could be assigned to be of metal phosphate, we attributed this peak to the presence of titanium phosphate. By increasing the P/Ti molar ratio to 2.06, (Fig. 2b) few weak peaks at 757 and 509.5 cm^{-1} appeared, the first peak is attributed to the deformation vibration of P–O–P [42] indicating the presence of pyrophosphate while the second one assigned as P–Cl stretching [37] and interpreted as traces of unreacted PCl$_3$ adsorbed or trapped inside the porous structure. While by increasing the temperature during the heat treatment from 500 °C for 10 h to 800 °C for 3 h, generally, the broad peaks changed into sharp peaks and some sub-peaks formed.

Sample P-c (Fig. 2c) shows bands around 2,344, 1,631, 1,209, 1,062, 982, and 924 cm^{-1} which are assigned as phosphorus acid, structural water, titanium phosphate or TOP, P=O [42], aliphatic P–O–C, and stretch vibration of P–OH (assigned to phosphate, oxide phosphate or pyrophosphate), respectively. On the other hand, sample P-d (Fig. 2d), shows bands positioned at around 2,344, 1,634, 1,074, 954, 743, 621, 565, and 449 cm^{-1} which were assigned as phosphorous acid, structural water, Ti–O–P skeletal stretching vibrations [32, 40, 41], phosphorus ester P–OH stretching [37], deformational vibration of P–O–P similar to this reported by Patnaik [42] who indicated the presence of TPP, bending vibrations of phosphate groups, respectively.
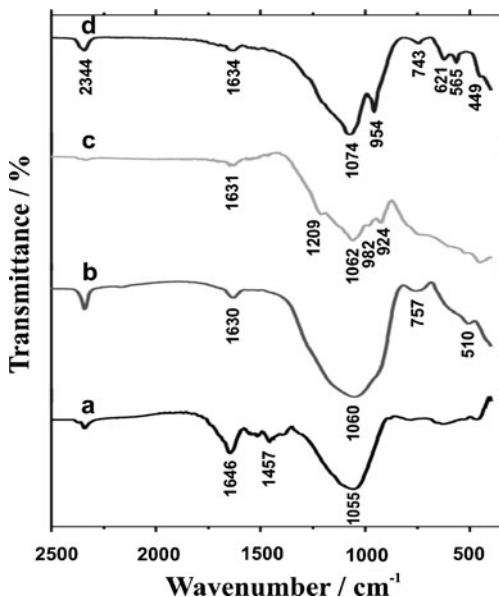

Fig. 2 FTIR spectra of titanium phosphate materials for samples prepared from P/Ti molar ratio of 0.412 (a) and of 2.06 (b) after heat treated at 500 °C for 10 h and of P/Ti molar ratio of 0.412 (c) and 2.06 (d) heat treated at 800 °C for 3 h. All heat treatment done in air

At 500 °C for 10 h, the synthesized materials (samples P-a and P-b) show the quasi-hexagonal (short-range-ordered mesoporous structure), as shown from SAXRD (Fig. 3a, b). The SAXRD shows only one single peak. The absence of any peak at higher angles indicated that walls of these materials are amorphous and lack of long-range order which suggested the presence of disordered hexagonal or wormhole type structure [28].

Our SAXRD is inconsistent with that of Fei et al. [43], where they claimed that the material they prepared is in the range of mesoporous–macroporous porous materials; however, there was no evidence from the SAXRD where there was no detectable diffraction peaks. The mesoporosity in their work can be evidenced only from the nitrogen adsorption isotherms they presented, while the pore–distribution curves they showed did not reveal any macroporous structure, instead, it confirmed the mesoporous structure, the TEM image showed as a proof of macroporous is misleading, instead, it showed channels between agglomerated particles and not pores as they claimed. The same issue of misleading evidence of mesoporous structure was reported in the work of Qiao et al. [44]. The quality of the SAXRD, in many cases of the titanium phosphate could be affected by the hygroscopic nature of the samples which might cause a difficulty of experimental measurements and affect the quality of the SAXRD peaks. Sample P-a (Fig. 3a) shows a reflection at 2θ of around 0.84° corresponding to a d-spacing of 10.48 nm, which we assigned to the average of the pore size of this material.

On the other hand, sample P-b (Fig. 3b) shows a reflection at 2θ of around 0.79° corresponding to the d-

spacing of 11.11 nm. This incremental shift in d-spacing upon increasing the P/Ti ratio of about 0.6 nm in the d-spacing shows that the material is still in the range of mesoporous material as identified by IUPAC classification of the porous materials. Thieme and Schueth [35] showed a similar shift of the d-spacing of as-received sample compared to sample calcined at 550 °C, the difference of the d-spacing was 0.4 nm, which is consistent with our results. They reported that the material is titanium oxo phosphate without giving an experimental evidence of the presence of this material. In our work, the formation of definite TOP phase could not be proved solely by XRD.

At the same heat-treatment conditions, WAXRD (Fig. 3c, d) sample P-a shows a crystalline phase indexed to anatase TiO_2 (Fig. 3d compared to JCPDS no. 71–1168, Fig. 3c) at the lowest P/Ti molar ratio used in this work. By increasing the molar ratio of the P/Ti, sample P-b, the characteristic peaks of anatase TiO_2 vanished except the main peak, at a value of 2θ of around 23.8° very close to 25.2° corresponds to (101) peak of anatase TiO_2. This peak's broadening and the absence of other peaks characteristic to TiO_2 suggesting that the material is amorphous anatase TiO_2, $(TiO)_2P_2O_7$ or TiP_2O_7 (Fig. 3e compared to Fig. 4f, g). It is obvious that by increasing the P/Ti molar ratio the formation of anatase–TiO_2 is suppressed by the increase of phosphorus amount compared to titanium ratio.

When introducing phosphate as additive into calcined TiO_2, transformation of anatase–TiO_2 into the most stable thermodynamic form, the rutile (provided that the average particle size diameter of TiO_2 is higher than 10 nm) [45, 46] is inhibited. The inhibition of anatase–rutile transformation by phosphorus was discussed early [47] and confirmed recently [48, 49], the transformation of anatase TiO_2 itself
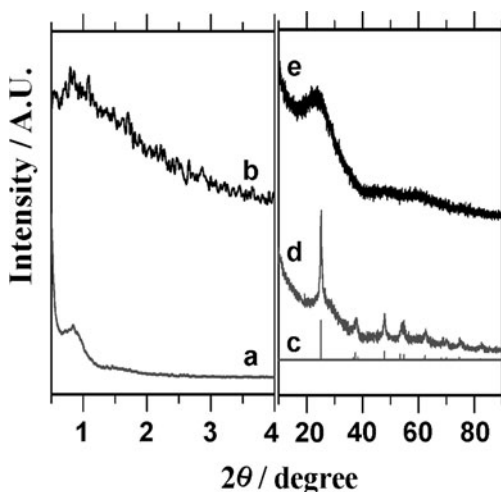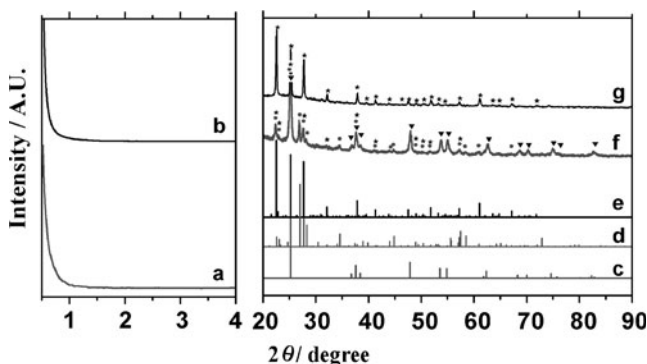

Fig. 3 SAXRD powder pattern of titanium phosphate materials of sample synthesized using P/Ti molar ratio of 0.412 (**a**) and 2.06 (**b**). WAXRD powder pattern of samples synthesized using P/Ti molar ratio of 0.412 (**d**) and 2.06 (**e**). Diffractogram (**c**) showing the JCPDS number 71–1168 corresponding to anatase TiO_2. All samples heat treated at 500 °C for 10 h in air

Fig. 4 SAXRD powder pattern of titanium phosphate materials of samples synthesized using P/Ti molar ratios of 0.412 (**a**) and 2.06 (**b**). WAXRD powder pattern of samples synthesized using P/Ti molar ratio of 0.412 (**f**) and 2.06 (**g**). Diffractograms **c**, **d** and **e** represent the JCPDS numbers 71-1168, 39-0207 and 38-1468 corresponding to anatase TiO_2, $(TiO)_2P_2O_7$ and TiP_2O_7, respectively. All samples heat treated at 800 °C for 3 h in air

might be retarded due to formation anatase–phosphate surface of the amorphous titanium oxide leading to suppress the crystal growth of the TiO_2 crystallite. The presence of phosphate on the surface of TiO_2 limits the growth of grains during calcination and suppresses the anatase–rutile transformation, while the presence of phosphate in bulk of TiO_2 promotes the anatase–rutile transformation [50]. After changing calcination conditions, from 500 °C for 10 h to 800 °C for 3 h (Fig. 4), the SAXRD (Fig. 4a, b) shows that the mesoporosity is lost completely, as indicated by the absence of any peaks attributed to the incomplete condensation of the wall [27].

On the other hand, WAXRD (Fig. 4c–g) showed completely different XRD patterns from those discussed in Fig. 3. P-c sample (Fig. 4f) even still showing the anatase TiO_2 as indexed by JCPDS no. 71–1168 (Fig. 4c) showed some other peaks which we identified as TOP of chemical formula $(TiO)_2P_2O_7$, as indexed by JCPDS no. 39–207 (Fig. 4d); however, the presence of a third phase of TiP_2O_7, JCPDS no. 38–1468 (Fig. 4e), could not be excluded in this sample. The phase purity of this material still need further confirmation which could not be attained exclusively from XRD patterns as mentioned above.

By increasing the P/Ti molar ratio, sample P-d (Fig. 4g), the relative concentration of TOP decreased as indicated by the increase of the peak signal intensity while those of the TPP increased. However, minor phase such as anatase TiO_2 might still present either as an amorphous or even crystalline phase in concentration behind the detection limit of the XRD technique.

At 800 °C for 3 h, the samples were affected obviously by increasing P/Ti molar ratio, and structural changes were observed. We believe that structural change occurred during TPP formation, and the structural change was from the tetragonal (anatase TiO_2) to orthorhombic (TOP), then to cubic (TPP) structure.

Figure 5 showed the discharge–charge curves of samples P-a to P-d at a constant current density of 20 mA g^{-1} at cutoff potentials between 1.5 and 3.5 V. The specific capacity of the materials prepared at 500 °C for 10 h (Fig. 5) decreased by increasing the P/Ti molar ratio. The specific capacities were ~137 mA h g^{-1} for sample P-a (Fig. 5a) and around 25 mA h g^{-1} for sample P-b (Fig. 5b) compared to a theoretical capacity of TiP_2O_7 of about 121 mA h g^{-1} (calculation based on one mole insertion of lithium); however, at this temperature, crystalline TiP_2O_7 single phase could not be confirmed as indicated from the WAXRD (Fig. 3). The very low capacity of sample P-b is attributed to its amorphous nature as shown above from XRD data. The low capacity of amorphous material is in agreement with the work of Wilhelm et al. [51]; however, most of the amorphous materials showed high
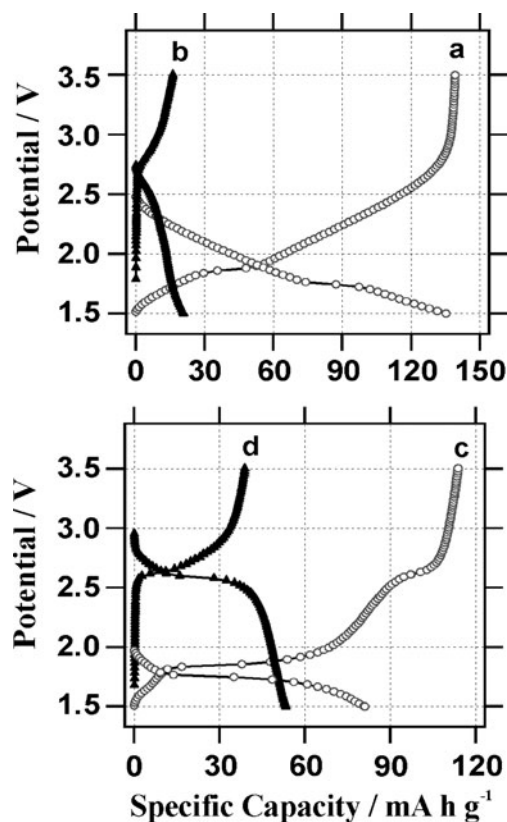

Fig. 5 The first cycle of charging–discharging capacities of titanium phosphate materials heat treated at 500 °C for 10 h in air, showing samples synthesized using P/Ti molar ratio of 0.412 (**a**) and 2.06 (**b**) and materials heat treated at 800 °C for 3 h in air showing samples synthesized using P/Ti molar ratio of 0.412 (**c**) and 2.06 (**d**). Current density used during charging–discharging was 20 mA g^{-1}

capacity when compared to crystalline one [52–55]. It is worth mentioning that Patoux et al. [56] synthesized TiP_2O_7; however, their work was not focusing on the mesoporous structure.

In this work, we did not notice any significant lithium-ion insertion into our amorphous sample, which can exclude the presence of amorphous anatase TiO_2 in that sample. Instead, mesoporous, polycrystalline anatase TiO_2 (Fig. 3a and d) is present, while mesoporous, amorphous phase developed when the P/Ti molar ratio increased (Fig. 3b and e). We anticipated this amorphous phase to be either TOP or amorphous TPP as discussed above.

The specific capacity of our prepared anatase TiO_2 of ~137 mA h g^{-1} (Fig. 5a) is in good agreement with the work of Kijima et al. [57], where they reported a value of 85 mA h g^{-1} (for the first discharge–charge cycle at 10 mA g^{-1} with a cutoff potential between 1 and 3 V) for thin flakes TiO_2, our prepared mesoporous material showing better capacities due to its stabilization by phosphate groups. On the other hand, our discharge capacity of ~137 mA h g^{-1} is better than the value

reported by Zhou et al. [58] for TiO_2 nanotubes of ~90 mA hg^{-1} prepared by the hydrothermal method (compared at the same cut-off potentials and at the same applied current density).

The increase of phosphorus content in the prepared materials resulted in a decrease in the specific capacity as it is shown in Fig. 5b to a value of about 25 mA hg^{-1}, this decrease indicated that amorphous TOP or TPP has been developed. The detection of polycrystalline anatase TiO_2 was a straightforward from the XRD results; moreover, lithium insertion electrochemistry confirmed its presence where sample P-a (Fig. 5a) showed a discharge plateau around 1.75 V corresponding to the insertion of lithium ions, and charge plateau around 1.86 V, corresponding to extraction of lithium ions, which is similar to that of pure anatase TiO_2 [59, 60]. However, Huang et al. [59] reported slightly different values of the insertion of 1.65 V and extraction of 1.95 V at 0.99 mA cm^{-2} These values shifted slightly to more positive values upon decreasing the applied current densities. Zotti et al. [61] reported lithium-ion insertion into amorphous titania at a potential around 0.5–0.6 V more negative than that of polycrystalline anatase, their results confirmed afterwards [62].

On the other hand, samples heat treated at 800 °C for 3 h (Fig. 5c and d), showed a decrease in specific capacities by increasing the phosphorous amount similar to the heat treatment of samples at 500 °C for 10 h. The specific capacity shows about 81 mA hg^{-1} for sample P-c (Fig. 5c) which decreased after increasing the P/Ti ratio for sample P-d (Fig. 5d) to about 53 mA hg^{-1}. This decrease in capacity from sample P-c to sample P-d is less than that for sample P-a to P-b (Fig. 5a and b), which is due to structure changes as shown above from the XRD data. Figure 5c showed three plateaux at 1.75, 1.9 and 2.6 V. The first two plateaux are typical characteristics for insertion and extraction of Li^+ into/from anatase TiO_2 structure, respectively. The extraction of lithium at higher redox potential showed as the third plateau at 2.6 V. The redox value corresponds to the presence of Ti^{4+}/Ti^{3+} in TiP_2O_7 [63]. The absence of the corresponding discharge plateau is unclear; however, a mixture of TiP_2O_7 and TiO_2 might present with a higher percent of the latter. By increasing the P/Ti molar ratio, the first two plateaux (Fig. 5d), raising a discharge and charge plateau of 2.6 V which is consistent with previous work [10, 56, 63] or even slightly shifted from these values [64].

Our experimental results suggest that the formation of the TiO_2, $(TiO)_2P_2O_7$ and/or TiP_2O_7 can be related to the amount of titanium and of phosphorous precursor used during the synthesis. The amount of phosphorus can affect directly the amount of the generated H_3PO_4

according to Eqs. 1–3, which can affect the amount of pyrophosphoric acid and its reaction with Ti precursor during the reaction. The cycleability of all synthesized materials for consecutive 20 cycles showed that the materials can be cycled without loss in the specific capacity (Fig. 6).

Figure 7 shows cyclic voltammograms P-a and P-b samples treated at 500 °C for 10 h (Fig. 7a and b), and samples P-c and P-d heat-treated at 800 °C for 3 h (Fig. 7c and d). At 500 °C for 10 h, the voltammogram (Fig. 7a) shows an insertion broad peak located at 2.56 V compared to its counterpart of extraction positioned at 2.82 V. We attributed these peaks to the presence of amorphous $(TiO)_2P_2O_7$ (vide supra) by sweeping the potential further to a more negative value; a relatively sharp peak found at 1.67 V assigned to insertion Li^+ into the anatase TiO_2 compared to its counterpart of extraction peak located at 2.04 V. The reported values in our work are lower than the values of around 1.75 and 1.95 V assigned respectively to insertion and extraction of lithium into anatase TiO_2 [65–67]. At 500 °C for 10 h, the increase in P/Ti molar ratio resulted in the vanishing of the anatase peak while a sharp peak positioned at 2.6 V prominently appeared.

The difference in the insertion and extraction peaks of the data we report in this work, to the best of our knowledge, is attributed to phosphate chemisorption on the surface of TiO_2 in place of hydroxyl groups which can affect the ionic mobility because of changing bidentate attachment [48], or to particle size contribution which might stimulate this potential shift. Subramanian
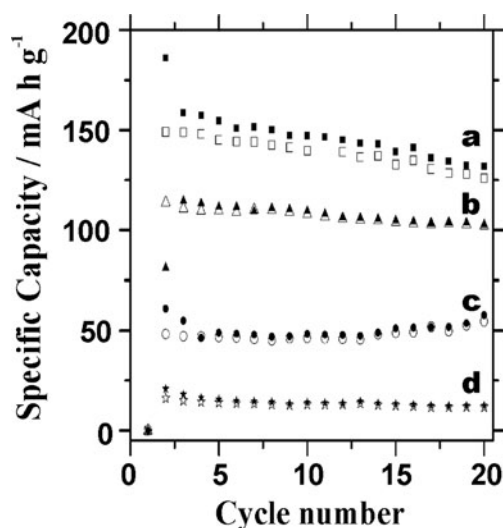
Fig. 6 Cycleability of materials synthesized at P/Ti molar ratios of 0.412 (a) and 2.06 (d) heated at 500 °C for 10 h in air and P/Ti molar ratios of 0.412 (b) and 2.06 (c) heated at 800 °C for 3 h in air. *Open marks* represent discharging while *filled marks* are charging

Fig. 7 Cyclic voltammetry of cathodes prepared from active materials from samples prepared using P/Ti molar ratios of 0.412 (**a**) 2.06 (**b**) heat treated at 500 °C for 10 h and using P/Ti molar ratios of 0.412 (**c**) 2.06 (**d**) heat treated at 800 °C for 3 h. The potential sweep starts at 3.6 to switching potential of 1.1 and then reversed to 3.6 V at a scan rate of 0.1 mV s^{-1}
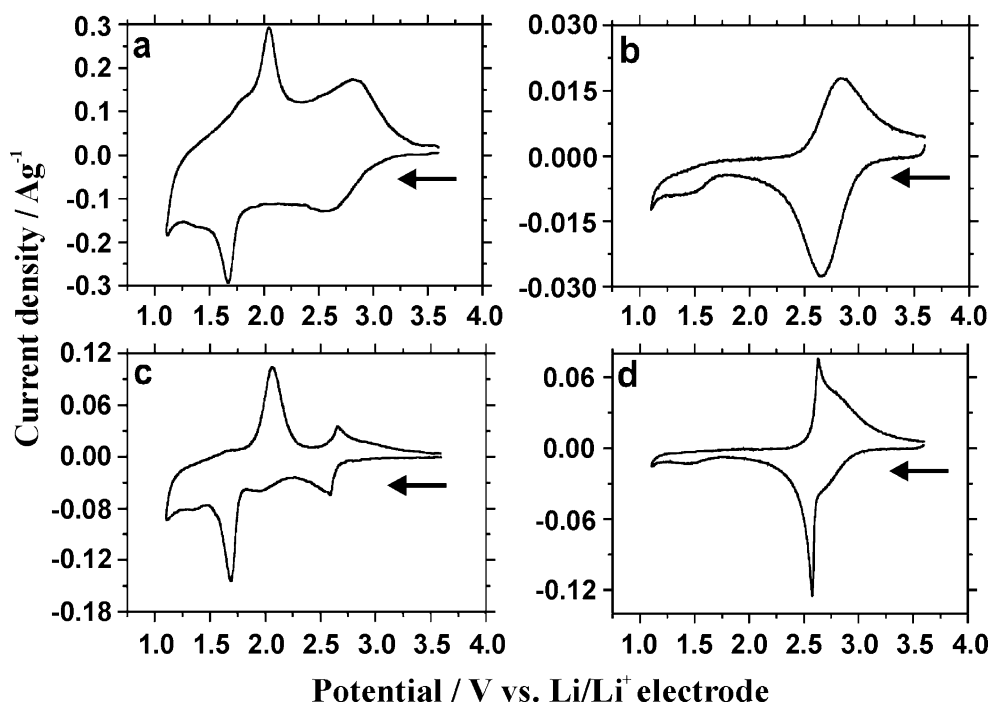
et al. [68] reported dependence of potential peak shift on particle size; in their work, they reported that decreasing the particle size to nanometer size resulted in cathodic (insertion) potential peak shift to a more positive value while anodic (extraction) potential peak shifted to a more negative value (at a scan rate of 0.1 mV s^{-1}). Based on this, our values of the potential peak suggested that we have a nano-TiO$_2$ even with a smaller particle size as described above [68]. Peak separations reported by Subramanian et al. [68] were 0.65 and 0.49 V corresponding respectively to micro- and nano-anatase TiO$_2$ particles, while in our work the peak separations are 0.38 and 0.375 V for samples P-a and P-c, respectively assigned to anatase TiO$_2$ in the presence of phosphate or pyrophosphate materials. In our work, crystallite sizes of samples P-a, P-c and P-d were 13.3, 26.7, and 64.5 nm, respectively as determined by analysis of peak broadening by using the Scherrer equation [69] and taking Si as a standard. While the particle size at 800 °C for 3 h was found to be dependant on the P/Ti molar ratio, the lattice strain was found to be inversely dependent on the P/Ti molar ratio. The reported values in our work are 1.34%, 0.74% and 0.37% for the P-a, P-c and P-d samples, respectively, which shows that the lattice strain was minimized for the TiP$_2$O$_7$ sample.

At 800 °C for 3 h, peak potentials were positioned at 2.58 V for insertion while positioned at 2.66 V for extraction (ΔE_p=0.08 V) for sample P-c. On the other hand, the peak potentials for sample P-d were positioned at 2.57 V for insertion of lithium ion and 2.63 V for lithium-

ion extraction (ΔE_p=0.06 V). The peaks of sample P-c were more broad compared to the sharp peaks of sample P-d where the all tetragonal (TiO$_2$) not converted fully to cubic (TiP$_2$O$_7$), which are dependent on the amount of P/Ti, once the P/Ti increased, all the tetragonal converted into cubic. The reported 2.6 V for insertion of lithium ion into TiP$_2$O$_7$ [63] is very similar to the value reported here in our work, the little shift of around 20–30 mV could be ascribed to the presence of mixed phase or due to the particle size changing which can have this effect as discussed above. At such a high temperature of 800 °C for 3 h, surprisingly, anatase TiO$_2$ still exists (sample P-c), which we ascribed to the stabilizing effect of phosphate ions and the inhibition effect of conversion into the rutile phase by phosphate, as discussed above. By increasing the P/Ti molar ratio, anatase disappeared completely and vestigial broad peak appeared around 1.38 V as a result of formation of traces of rutile TiO$_2$ [70], this rutile traces could not be detected by XRD.

The lithiation or intercalation into the anatase TiO$_2$ structure can occur according to general reaction:

$$TiO_2 + xLi^+ + xe^- \rightleftarrows Li_xTiO_2$$
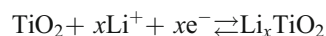
Sample P-a showed the same peak for anatase TiO$_2$ as that for the heat-treated samples at 500 °C for 10 h; however, the redox peaks converted into sharp peaks by increasing the heat treatment. By increasing the P/Ti molar ratio, sample P-b showed two main peaks around 1.7 and 2.6 V which were assigned to anatase TiO$_2$ and TPP, respectively, as confirmed by XRD. However, XRD could

not confirm the presence of pure phase because the strongest signals of the phases are common in these phases. Cyclic voltammetry confirmed that sample P-b is a pure TPP, which could not be assured solely by XRD. Sample P-d showed sharp CV peaks compared to amorphous ones which indicated its high crystalline formation of TiP_2O_7 as confirmed by XRD.

The morphologies of different particles were depicted in Fig. 8. At 500 °C for 10 h, sample P-a shows pores on the surface with an average diameter of around 23 nm. However, since particle aggregation might be misleading, this should be considered only as approximation. For
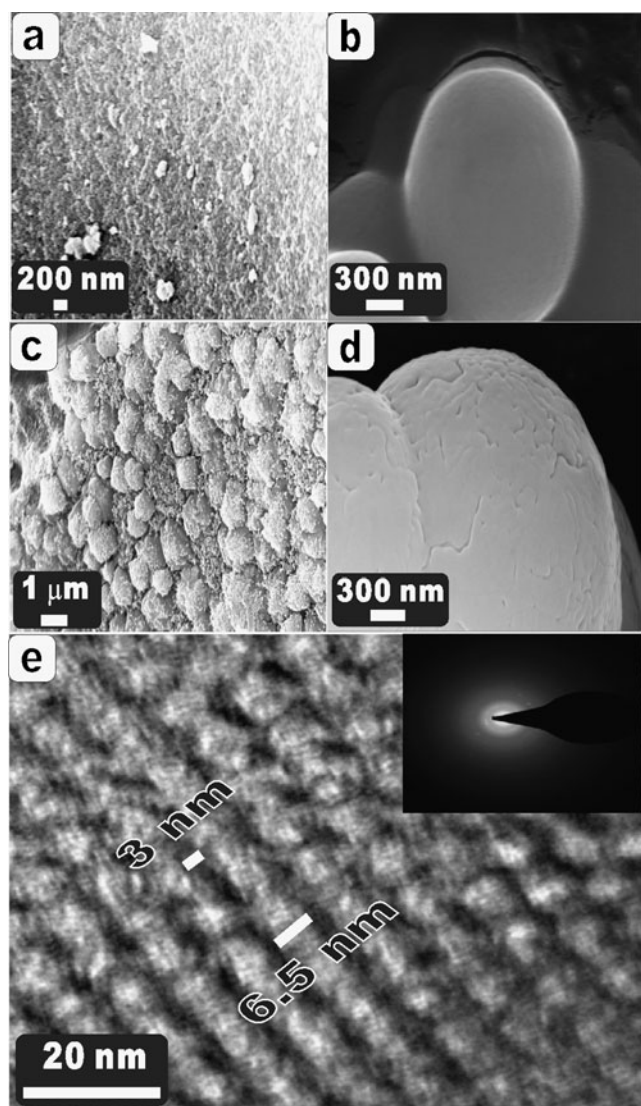

Fig. 8 Representative graphs of SEM of the synthesized samples after heat treatment at 500 °C for 10 h in air using P/Ti molar ratio of 0.412 (**a**) and 2.06 (**b**) and of heat treatment of 800 °C for 3 h in air for samples synthesized using P/Ti molar ratio of 0.412 (**c**) and 2.06 (**d**). HRTEM of sample synthesized from P/Ti=0.412 followed by heat treatment at 500 °C for 10 h, showing the mesoporous arrangement and wall of pores (**e**), *inset* showing SAED

sample P-b, spherical aggregated particles. At 800 °C for 3 h, sample P-c shows an array of particles, which we believe is a form of a mixture of TiO_2 and TiP_2O_7 as confirmed above from cyclic voltammetry, charge–discharge and XRD data. By increasing the molar ratio, sample d shows particles attributed to formation of TiP_2O_7. These particles show some zigzag-like grooves on its surface.

Figure 8e, sample P-a, shows the repeated spacing (sum of wall and pore sizes) of ca. 9.5 nm, close to the value from SAXRD (ca. 10.48 nm; Fig. 3a); the former is more precise since the XRD peak at 0.84° is very broad. The pore size was estimated to be ca. 6.5 nm and its wall thickness of 3 nm. The SAED image shows that this material possesses poorly crystalline wall instead of amorphous one, which is consistent with the characterization by WAXRD.

Conclusions

The mesoporous TP materials were stable up to 500 °C for 10 h in our experimental conditions; the mesoporosity lost after heat treatment at 800 °C for 3 h. The FTIR, XRD, lithium insertion electrochemistry, all proved that TPP has a less capacity compared to a mixture of titanium oxide and TOP. However, TiP_2O_7 has a flat potential which can be related to the battery application which needs constant current drain and of moderate power. The molar ratio of P/Ti and heat treatment affected the purity of the phase produced of TP and hence affected other electrochemical properties and morphology of particles, while low P/Ti molar ratio concentration favored formation of stable anatase TiO_2, with traces of rutile undetectable with XRD, the high P/Ti molar ratio favored the formation of TiP_2O_7 at high temperature (800 °C for 3 h) with zero strain for the lattice. At moderate temperature (500 °C for 10 h), a mixture of titanium oxo phosphate and TiP_2O_7 formed. The morphologies of the TiP_2O_7 materials vary during synthesis where it is dependent on the P/Ti molar ratio and temperature which required to complete the synthesis process. Spherical particles formed for the TiP_2O_7 at P/Ti=2.06 at 800 °C for 3 h, while at 500 °C for 10 h, a combination of TiO_2, titanium oxo phosphate and TiP_2O_7 can form spheres only when P/Ti molar ratio is high. At lower temperature (500 °C for 10 h) and lower P/Ti molar ratio (0.421), sample (a) showed the best capacity; however, upon cycling, this capacity faded. On the other hand, at a higher temperature (800 °C for 3 h), and at lower P/Ti molar ratio (0.421), sample (b) showed the best behavior, where the capacity is not faded compared to sample (a).

References

1. Kresge CT, Leonowicz ME, Roth WJ, Vartuli JC, Beck JS (1992) Ordered mesoporous molecular sieves synthesized by a liquid-crystal template mechanism. Nature 359:710–712

2. Beck JS, Vartuli JC, Roth WJ, Leonowicz ME, Kresge CT, Schmitt KD, Chu CT-W, Olson DH, Sheppard EW, McCullen SB, Higgins JB, Schlenker JL (1992) A new family of mesoporous molecular sieves prepared with liquid crystal templates. J Am Chem Soc 114:10834–10843

3. Yu JC, Zhang L, Zheng Z, Zhao J (2003) Synthesis and Characterization of Phosphated Mesoporous Titanium Dioxide with High Photocatalytic Activity. Chem Mater 15:2280–2286

4. Zhao J, Tian B, Yue Y, Hua W, Zhao D, Gao Z (2005) New catalysts for dichlorodifluoromethane hydrolysis: Mesostructured titanium and aluminum phosphates. J Mol Cat A: Chem 242:218–223

5. Gianotti E, Oliveira EC, Coluccia S, Pastore HO, Marchese L (2003) Synthesis and surface properties of Ti-containing mesoporous aluminophosphates. A comparison with Ti-grafted mesoporous silica Ti-MCM-41. Inorg Chim Acta 349:259–264

6. Yantasee W, Deibler LA, Fryxell GE, Timchalk C, Lin Y (2005) Screen-printed electrodes modified with functionalized mesoporous silica for voltammetric analysis of toxic metal ions. Electrochem Commun 7:1170–1176

7. Attia A, Zukalova M, Pospisil L, Kavan L (2007) Electrochemical impedance spectroscopy of mesoporous Al-stabilized TiO$_2$ (anatase) in aprotic medium. J Solid State Electrochem 11:1163–1169

8. Attia A, Zukalova M, Rathousky J, Zukal A, Kavan L (2005) Mesoporous electrode material from alumina-stabilized anatase TiO$_2$ for lithium ion batteries. J Solid State Electrochem 9:138–145

9. Kavan L, Attia A, Lenzmann F, Elder SH, Grätzel M (2000) Lithium insertion into zirconia-stabilized mesoscopic TiO$_2$ (anatase). J Electrochem Soc 147:2897–2902

10. Shi Z, Wang Q, Ye W, Li Y, Yang Y (2006) Synthesis and characterization of mesoporous titanium pyrophosphate as lithium intercalation electrode materials. Micropor Mesopor Mat 88:232–237

11. Kapoor MP, Inagaki S, Yoshida H (2005) Novel zirconium-Titanium Phosphates Mesoporous Materials for Hydrogen Production by Photoinduces Water Splitting. J Phys Chem B 109:9231–9238

12. Sreethawong T, Puangpetch T, Chavadej S, Yoshikawa S (2007) Quantifying influence of operational parameters on photocatalytic H$_2$ evolution over Pt-loaded nanocrystalline mesoporous TiO$_2$ prepared by single-step sol-gel process with surfactant template. J Power Sources 165:861–869

13. Jia X, He W, Luo S, Feng Y, Xu G, Li H, Zhang X (2006) Mesoporous anatase with multi-morphologies synthesized by sol-gel method. Mater Lett 60:1839–1842

14. Hu X, Skadtchenko BO, Trudeau M, Antonelli DM (2006) Hydrogen storage in chemically reducible mesoporous and microporous Ti oxides. J Amer Chem Soc 128:11740–11741

15. Deepa M, Srivastava AK, Sood KN, Agnihotry SA (2006) Nanostructured mesoporous tungsten oxide films with fast kinetics for electrochromic smart windows. Nanotechnology 17:2625–2630

16. Jheong HK, Kim YJ, Pan JH, Won TY, Lee WI (2006) Electrochromic property of the viologen-anchored mesoporous TiO$_2$ films. J Electroceram 17:929–932

17. Oregan B, Grätzel M (1991) A Low-Cost, High-Efficiency Solar-Cell Based on Dye-Sensitized Colloidal TiO$_2$ Films. Nature 353:737–740

18. Grätzel M (2005) Mesoscopic solar cells for electricity and hydrogen production from sunlight. Chem Lett 34:8–13

19. Hagfeldt A, Grätzel M (2000) Molecular photovoltaics. Accounts Chem Res 33:245–250

20. Padhi AK, Nanjundaswamy KS, Masquelier C, Goodenough JB (1997) Mapping of Transition Metal Redox Energies in Phosphates with NASICON Structure by Lithium Intercalation. J Electrochem Soc 144:2581–2586

21. Padhi AK, Nanjundaswamy KS, Masquelier C, Okada S, Goodenough JB (1997) Effect of Structure on the Fe^{3+}/Fe^{2+} Redox Couple in Iron Phosphates. J Electrochem Soc 144:1609–1613

22. Padhi AK, Nanjundaswamy KS, Goodenough JB (1997) Phospho-olivines as Positive-Electrode Materials for Rechargeable Lithium Batteries. J Electrochem Soc 144:1188–1194

23. Ellis B, Kan WH, Makahnouk WRM, Nazar LF (2007) Synthesis of nanocrystals and morphology control of hydrothermally prepared LiFePO$_4$ 7. J Mater Chem 17:3248–3254

24. Herle PS, Ellis B, Coombs N, Nazar LF (2004) Nano-network electronic conduction in iron and nickel olivine phosphates 1. Nat Mater 3:147–152

25. Ramana CV, it-Salah A, Utsunomiya S, Becker U, Mauger A, Gendron F, Julien CM (2006) Structural characteristics of lithium nickel phosphate studied using analytical electron microscopy and Raman spectroscopy 8. Chem Mater 18:3788–3794

26. Saidi MY, Barker J, Huang H, Swoyer JL, Adamson G (2002) Electrochemical properties of lithium vanadium phosphate as a cathode material for lithium-ion batteries 2. Electrochem Solid State Lett 5:A149–A151

27. Antonelli DM (1999) Synthesis of phosphorus-free mesoporous titania via templating with amine surfactants. Micropor Mesopor Mat 30:315–319

28. Santos-Pena J, Soudan P, Cruz-Yusta M, Franger S (2006) Increasing the electrochemical activity of transition metal phosphates in lithium cells by treatment with intimate carbon: The case of titanium phosphate. Electrochim Acta 51:4841–4849

29. Yang JS, Xu JJ (2006) Synthesis and characterization of carbon-coated lithium transition metal phosphates LiMPO$_4$ (M = Fe, Mn, Co, Ni) prepared via a nonaqueous sol-gel route. J Electrochem Soc 153:A716–A723

30. Alberti G, Casciola M, Cavalaglio S, Vivani R (1999) Proton conductivity of mesoporous zirconium phosphate pyrophosphate. Solid State Ionics 125:91–97

31. Rodriguez-Castellon E, Jimenez-Jimenez J, Jimenez-lopez A, Maireles-Torres P, Ramos-Barrado JR, Jones DJ, Roziere J (1999) Proton Conductivity of Mesoporous MCM type of Zirconium and Titanium Phosphates. Solid State Ionics 125:407–410

32. Bhaumik A, Inagaki S (2001) Mesoporous titanium phosphate molecular sieves with ion-exchange capacity. J Am Chem Soc 123:691–696

33. Serre C, Taulelle F, Ferey G (2002) Synthesis and Characterization of New Lamellar Templated Titanium(IV) Phosphates with Perforated Layers: MIL-28$_n$ or Ti$_3$O$_2$X$_2$(HPO$_4$)$_x$(PO$_4$)$_y$.(N$_2$C$_n$H$_{2n+6}$)$_z$.(H$_2$O)$_2$ (n = 2, 3; x = 0, 2; y = 4, 2; z = 3, 2; X = F, OH). Chem Mater 14:998–1003

34. Pan C-L, Zhang W-X, Wang Y-L, Zhou Z, Jiang D-Z, Wu S-J, Wu T-H (2003) Synthesis of Mesoporous Titanium Phosphate with High Surface Area Using Long-Chain Alkylamine. Mater Lett 57:3815–3819

35. Thieme M, Schueth F (1999) Preprartion of a Mesoporous High Surface Area Titanium Oxo Phosphate via a Non-Ionic Surfactant Route. Micropor Mesopor Mat 27:193–200

36. Kovalchuk TV, Sfihi H, Korchev AS, Kovalenko AS, Il'in VG, Zaitsev VN, Fraissard J (2005) Synthesis, Structure, and Acidic Properties of MCM-41 Functionalized with Phosphate and Titanium Phosphate Groups. J Phys Chem B 109:13948–13956

37. Stuart BH (2004) Infrared spectroscopy: fundamentals and applications. Wiley, Chichester

38. Jones P, Hockey JA (1971) Infra-Red Studies of Rutile Surfaces .2. Hydroxylation, Hydration and Structure of Rutile Surfaces. Trans Faraday Soc 67:2679–2685

39. Tarafdar A, Panda AB, Pradhan NC, Pramanik P (2006) Synthesis of spherical mesostructured zirconium phosphate with acidic properties. Micropor Mesopor Mat 95:360–365

40. Santos-Pena J, Cruz-Yusta M, Soudan P, Franger S, Cuart-Pascual JJ (2006) Carbon and transition metal containing titanium phosphates as electrodes for lithium ion batteries. Solid State Ionics 177:2667–2674

41. Pan C-L, Yuan S, Zhang W-X (2006) A neutral templating route to mesoporous titanium phosphate molecular sieves with enhanced thermal stability. Appl Cat A 312:186–193

42. Patnaik P (2004) Dean's analytical chemistry handbook. McGraw Hill, New York

43. Fei H, Zhou X, Zhou Z, Shen Z, Sun P, Yuan Z, Chen T (2007) Facile template-free synthesis of meso-macroporous titanium phosphate with hierarchical pore structure. Micropor Mesopor Mat 100:139–145

44. Qiao H, Xiao L, Zhang L (2008) Phosphatization: A promising approach to enhance the performance of mesoporous TiO$_2$ anode for lithium ion batteries. Electrochem Commun 10:616–620

45. Gribb AA, Banfield JF (1997) Particle size effects on transformation kinetics and phase stability in nanocrystalline TiO$_2$. Amer Mineral 82:717–728

46. Zhang HZ, Banfield JF (1998) Thermodynamic analysis of phase stability of nanocrystalline titania. J Mater Chem 8:2073–2076

47. Criado J, Real C (1983) Mechanism of the Inhibiting Effect of Phosphate on the Anatase-Rutil Transformation Inducted by Thermal and Mechanical Treatment of TiO$_2$. J Chem Soc, Faraday Trans 1(79):2765–2771

48. Grzmil B, Rabe M, Kic B, Lubkowski K (2007) Influence of Phosphate, Potassium, Lithium, and Aluminium on the Anatase-Rutile Phase Transformation. Ind Eng Chem Res 46:1018–1024

49. Grzmil B, Kic B, Rabe M (2004) Inhibition of the anatase - Rutile phase transformation with addition of K$_2$O, P$_2$O$_5$, and Li$_2$O. Chem Pap-Chem Zvesti 58:410–414

50. Gesenhues U (2001) Calcination of Metatitanic acid to titanium dioxide white pigments. Chem Eng Technol 24:685–694

51. Wilhelm O, Pratsinis SE, de Chambrier E, Crouzet M, Exnar I (2004) Electrochemical performance of granulated titania nanoparticles. J Power Sources 134:197–201

52. Wang X, Yang X, Zheng H, Jin J, Zhang Z (2005) Synthesis and electrochemical performance of amorphous hydrated iron phosphate nanoparticles. J Cryst Growth 274:214–217

53. Fang HT, Liu M, Wang DW, Sun T, Guan DS, Li F, Zhou JG, Sham TK, Cheng HM (2009) Comparison of the rate capability of nanostructured amorphous and anatase TiO$_2$ for lithium insertion using anodic TiO$_2$ nanotube arrays. Nanotechnology 20(22):225701

54. Furukawa H, Hibino M, Honma I (2004) Electrochemical properties of nanostructured amorphous, sol-gel-synthesized TiO$_2$/acetylene black composite electrodes. J Electrochem Soc 151:A527–A531

55. Huang X, Yue H, Attia A, Yang Y (2007) Preparation and Properties of Manganese Oxide/Carbon Composites by Reduction of Potassium Permanganate with Acetylene Black. J Electrochem Soc 154:A26–A33

56. Patoux S, Masquelier C (2002) Lithium Insertion into Titanium Phosphates, Silicates, and Sulfates. Chem Mater 14:5068

57. Kijima N, Takahashi Y, Hayakawa H, Awaka J, Akimoto J (2008) Synthesis, characterization, and electrochemical properties of a thin flake titania fabricated from exfoliated nanosheets. J Phys Chem Solids 69:1447–1449

58. Zhou YK, Cao L, Zhang FB, He BL, Li HL (2003) Lithium insertion into TiO$_2$ nanotube prepared by the hydrothermal process. J Electrochem Soc 150:A1246–A1249

59. Huang SY, Kavan L, Exnar I, Grätzel M (1995) Rocking Chair Lithium Battery Based on Nanocrystalline TiO$_2$ (Anatase). J Electrochem Soc 142:L142–L144

60. Xu JW, Ha CH, Cao B, Zhang WF (2007) Electrochemical properties of anatase TiO$_2$ nanotubes as an anode material for lithium-ion batteries 12. Electrochim Acta 52:8044–8047

61. Zotti G, Schiavon G, Zecchin S (1999) Anodic dissolution of titanium in acetonitrile to Ti(IV) perchlorate and subsequent reductive electrodeposition of amorphous TiO$_2$ films. J Electrochem Soc 146:637–641

62. Kavan L, Rathousky J, Grätzel M, Shklover V, Zukal A (2000) Surfactant-templated TiO$_2$ (Anatase): Characteristic Features of lithium Insertion Electrochemistry in Organized Nanostructures. J Phys Chem B 104:12012–12020

63. Uebou Y, Okada S, Egashira M, Yamaki J-I (2002) Cathode properties of pyrophosphates for rechargeable lithium batteries. Solid State Ionics 148:323–328

64. Kishore MS, Pralong V, Caignaret V, Varadaraju UV, Raveau B (2007) Electrochemical intercalation of lithium in the titanium hydrogeno phosphate Ti(HPO$_4$)$_2$•H$_2$O. J Power Sources 169:355–360

65. Kavan L, Grätzel M, Rathousky J, Zukal A (1996) Nanocrystalline TiO$_2$ (anatase) electrodes: Surface morphology, adsorption, and electrochemical properties. J Electrochem Soc 143:394–400

66. Lindstrom H, Sodergren S, Solbrand A, Rensmo H, Hjelm J, Hagfeldt A, Lindquist SE (1997) Li+ ion insertion in TiO$_2$ (anatase) .1. Chronoamperometry on CVD films and nanoporous films. J Phys Chem B 101:7710–7716

67. van de Krol R, Goossens A, Schoonman J (1999) Spatial extent of lithium intercalation in anatase TiO$_2$. J Phys Chem B 103:7151–7159

68. Subramanian V, Karki A, Gnanasekar KI, Eddy FP, Rambabu B (2006) Nanocrystalline TiO$_2$ (anatase) for Li-ion batteries. J Power Sources 159:186–192

69. Scherrer P (1918) Estimation of the size and internal structure of colloidal particles by means of röntgen Rays. Nachr Ges Wiss Göttingen 2:96–100

70. Milne NA, Skyllas-Kazacos M, Luca V (2009) Crystallite Size Dependence of Lithium Intercalation in Nanocrystalline Rutile. J Phys Chem C 113:12983–12995